MATER. RES. LETT.
2023, VOL. 11, NO. 10, 797–805
https://doi.org/10.1080/21663831.2023.2243990

MATERIALS RESEARCH LETTERS
Taylor & Francis
Taylor & Francis Group

ORIGINAL REPORTS

The potential benefit of pseudo high thermal conductivity for laser powder bed fusion additive manufacturing

Huan Ding, Selami Emanet, Yehong Chen and Shengmin Guo

Department of Mechanical and Industrial Engineering, Louisiana State University, Baton Rouge, LA, USA

ABSTRACT

This study examined the impact of transient pseudo high thermal conductivity to the fabrication of crack-free parts with Laser Powder-Bed-Fusion (L-PBF) based additive manufacturing (AM) method. Thermal diffusivity and thermal conductivity of L-PBF samples made by mixtures of IN939 alloy and Si powders were investigated. At temperatures above 800°C, the as-fabricated Si-doped IN939 was observed to exhibit an exceptionally high thermal conductivity, which can be attributed to the occurrence of endothermic reactions. This pseudo high thermal conductivity can effectively minimize the thermal stress and offers a potential solution to produce crack-free L-PBF parts for nonweldable alloys.

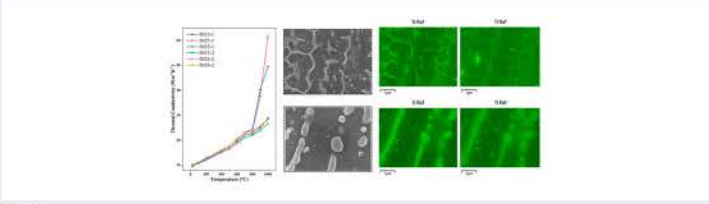

IMPACT STATEMENT

The paper proposes a potential solution for preparing crack-free L-PBF nonweldable alloys. Modifying the composition to introduce an endothermic reaction has been shown to decrease the tendency of cracking.

ARTICLE HISTORY
Received 17 May 2023

KEYWORDS
Laser powder bed fusion; Inconel 939; Crack-free; Endothermic reaction; Thermal stress

1. Introduction

In the Laser Powder-Bed-Fusion (L-PBF) additive manufacturing (AM) field, material thermal properties are crucial for both the fabrication process and the applications of the L-PBF parts. For example, by altering heat conduction [1, 2], the melt pool characteristics, temperature gradient [3], and thermal stress distribution can be significantly modified. However, the intricate thermodynamic behavior within the melt pool presents a challenge for researchers to monitor it in real-time. Consequently, there is insufficient research to establish a direct relationship between the thermal changes in the melt pool and the formation of hot cracks. Hot cracking is one of the main issues during the L-PBF, which is also a primary defect that limits the application of materials. Although many alloy systems have already been successfully commercialized [4–8], more than 5,000 alloys currently in use are unsuitable for L-PBF due to unfavorable melting and solidification dynamics, especially for Inconel alloys. Many Inconel alloys exhibit poor weldability [9] due to the formation of high-dense defects (hot cracks) [10, 11] during the L-PBF process. The constraints imposed by the limited availability of materials significantly impede the wide adoption of additive manufacturing technologies. Therefore, there is a pressing need to identify and implement effective solutions to this issue.

Hot cracking usually occurs when two conditions are combined: the presence of (i) a weak region (i.e. liquid film [12]) and (ii) significant thermal stress [13]. Considerable research effort has been devoted to addressing the issue of weak microstructural regions in metallic materials, and numerous theories have been proposed in the literature. These include the Rappaz-Drezet-Gremaud (RDG) criterion [14] and the thermal crack susceptibility index [15]. Despite the advancements achieved in the investigation of composition modification across various alloy systems, such as Al7075 alloy[16], IN738 alloy [17], and 316L stainless steel [18]. These studies have demon-

CONTACT Huan Ding hding3@lsu.edu Department of Mechanical and Industrial Engineering, Louisiana State University, Baton Rouge, LA 70803, USA; Shengmin Guo sguo2@lsu.edu Department of Mechanical and Industrial Engineering, Louisiana State University, Baton Rouge, LA 70803, USA

strated the effect of heterogenous nucleation caused by the addition of elements, resulting in a transition from columnar grains to equiaxed grains. However, the range of available nucleating agents is relatively narrow, which limits the ability to further improve the specific mechanical properties of the alloy. Also, the restricted accessibility and exorbitant expense of pre-alloyed powders impose limitations on the flexibility and affordability of additive manufacturing for new alloys.

Another efficacious method to enhance cracking resistance is to mitigate thermal stress during the printing procedure. Thermal stress in L-PBF parts is caused by the pronounced temperature gradient. A few researchers have directed their attention toward the pre-heating of substrate [19, 20]. Despite the resolution of the cracking issue, the elimination of the large-scale thermal gradient resulted in a reduction of the strengthening effect brought about by rapid cooling. This may lead to the deterioration of the sample's performance. Therefore, a new method is required to balance the reduction of thermal stress and strengthening of the properties.

In recent years, in-situ alloying in AM has emerged as a popular research direction [21]. The aim is to use a mixture of pure elemental powders instead of pre-alloyed powders in additive manufacturing processes to overcome the limitations of narrow composition ranges and high cost associated with pre-alloyed powders. By utilizing pure elemental mixtures, researchers can achieve a broader range of alloy compositions and reduce the overall material costs in the production of AM samples. However, it is true that using mixtures of multiple types of powders with different densities in an elemental mixture can lead to uneven flow under laser irradiation, potentially resulting in inaccurate alloy compositions. In our previous research [22], we reported the successful fabrication of a nearly crack-free Si-modified In939 alloy with a highly homogeneous composition. We utilized a two-powder mixture system consisting of pre-alloyed IN939 powder and pure Si powder. The blending process was conducted using a turbo-mixing method. Notably, we extended the mixing time to 10 h to ensure thorough mixing and achieve a uniform distribution of the Si modifier within the alloy matrix. This extended mixing duration played a crucial role in achieving the desired level of compositional homogeneity and minimizing the occurrence of cracks in the final printed parts.

Currently, in-situ alloying in the context of the L-PBF process is predominantly studied in aluminum alloys and titanium alloys [23]. There is scarce research on in-situ alloying of nickel-based alloys in this field. It has been proven that Si has a strong positive effect on eliminating hot cracks in Al alloys prepared by L-PBF [24–26]. The mechanism of crack elimination by Si addition in the Aluminum alloy is the traditional heterogeneous nucleation and Columnar-Equiaxed-Transition (CET) theory. However, some researchers have pointed out that the addition of Si increases the tendency of hot cracking in L-PBF nickel-based alloys [27–31]. In our previous study, we examined the design of a crack-free laser additive manufactured IN939 alloy with Si addition, and the addition of Si has shown minimal influence on grain refinement, and no significant CET phenomenon has been observed [22]. Considering that our research uses non-pre-alloyed powders, we believe that a new mechanism is responsible for weakening the thermal stresses. We hypothesized that the added Si reacted with the IN939 matrix in the molten pool. This endothermic phase transition may temporarily promote the specific heat/thermal conductivity in the high-temperature zone during the L-PBF process. This pseudo high thermal conductivity may reduce the temperature gradient around the laser scanning tracks. By reducing thermal stress in the high-temperature weak regions, cracking can be prevented. In this study, we directly measured the thermal properties of the modified IN939 as-fabricated samples, which were IN15(IN939 with 1.5 wt.% Si), IN25 (IN939 with 2.5 wt.% Si), and IN35 (IN939 with 3.5 wt.% Si). By studying the impact of endothermic reaction on thermal conductivity, this paper provides a new solution for making crack-free L-PBF parts using typically nonweldable alloys, such as high entropy alloy [32], with endothermic reaction agent addition. The method we proposed can be applied to a diverse selection of nonweldable alloys.

2. Materials and methods

Gas atomized IN939 powder was purchased from Carpenter Additive (USA). The powder consists of Ni (balance), Cr (25.0%), Co (15.0%), Ti (3.3%), Al (3.3%), C ($< 0.2\%$), Nb (0.9%), Ta (1.7%), W (2.7%), Si (0.03%), in weight percent. The size range of IN939 powder is 15 μm – 50 μm. Silicon powder was purchased from Alfa Aesar (USA), and the average size is about 4.5 μm. The purity of flake-shaped silicon powder is approximately 99.5%. Pure IN939 with Si powder was mixed in a SPEX 8000 m MIXER for 10 h.

Additive manufacturing of the pure IN939 and functionalized 939 with Si powders were performed on a team-built L-PBF machine. We applied a set of laser parameters based on the previous study [33], where the layer thickness (t) is 0.05 mm, the laser power (P) is 160 W, the laser scan speed (v) is 100 mm/s, and the hatch space (h) is 0.05 mm, respectively. Previous research has convincingly shown that pure IN939 exhibits favorable compactness and low porosity when exposed to

the high laser energy density currently employed. Moreover, the occurrence of keyhole-mode melting has not been detected. To minimize chemical inhomogeneity during Si-modified in-situ alloying, we have consistently employed this high laser energy density parameter set, also for the purpose of facilitating direct comparison with pure IN939 data obtained previously. The printing process was completed under a flowing argon atmosphere.

ANSYS finite-element model was employed. Heat flux with Gaussian distribution was applied to the metal block. The material thermal properties were based on the measured data. The mesh size is 100 µm and the time step is 2.5 ms. The Calculation of Phase Diagrams (CALPHAD) software Thermo-Calc was adopted for the Scheil Simulation. Mounted samples were observed with Scanning Electron Microscopy (SEM), Electron Backscatter Diffraction (EBSD). Also, X-Ray Diffraction (XRD) was employed to explore the phases of the samples. Differential Scanning Calorimetry (DSC) is performed on a NETZSH DSC 404 F1 system. The thermal properties are measured by a NETZSH LFA 467 HyperFlash system. The waterless Kalling's reagent was adopted for metallographic etching.

3. Results and discussion

Figure 1a shows SEM images of mechanically mixed IN939 pre-alloy powder and pure Si powder. Figure 1b shows the laser scanning strategys and the sample size. Figure 1c shows the melt pool information of the as-fabricated IN15 and IN35 etched cross-sections. The depths of 30 randomly selected molten pool structures were measured. The melt poor depth of IN15 is 60.5 ± 3.7 µm, and the melt poor depth of IN35 is 51.2 ± 4.3 µm. The shape of the molten pool changed from deep to shallow with the addition of Si. The inverse pole figures illustrate a favored crystallographic orientation of 001 < 100 > in IN939. It has been noted that the degree of this texture diminishes in tandem with the augmented concentration of silicon. Simultaneously, there is a reduction in the propensity for selective orientation and a rise in the proportion of high-angle grain boundaries. The microstructure features shown in Figure 1e indicate the possibility of a reduction of the thermal gradient.

The Netzsch LFA-467 system [34] measures thermal diffusivity directly and provides specific heat (C_p) calculations by comparing it with a reference sample. Thermal conductivity is the product of thermal diffusivity, specific heat, and density. The calculation equations are shown below:

$$C_{pr} * m_r * \Delta T_r = C_{pi} * m_i * \Delta T_i \quad (1)$$

$$K = C_p * \alpha * \rho \quad (2)$$

Where the m is the mass of the sample, ΔT is the maximum temperature rise of the sample during the flash shot in different testing temperatures. α is the measured thermal diffusivity, and ρ is the density of the sample. Subscripts r and i present the reference sample and tested

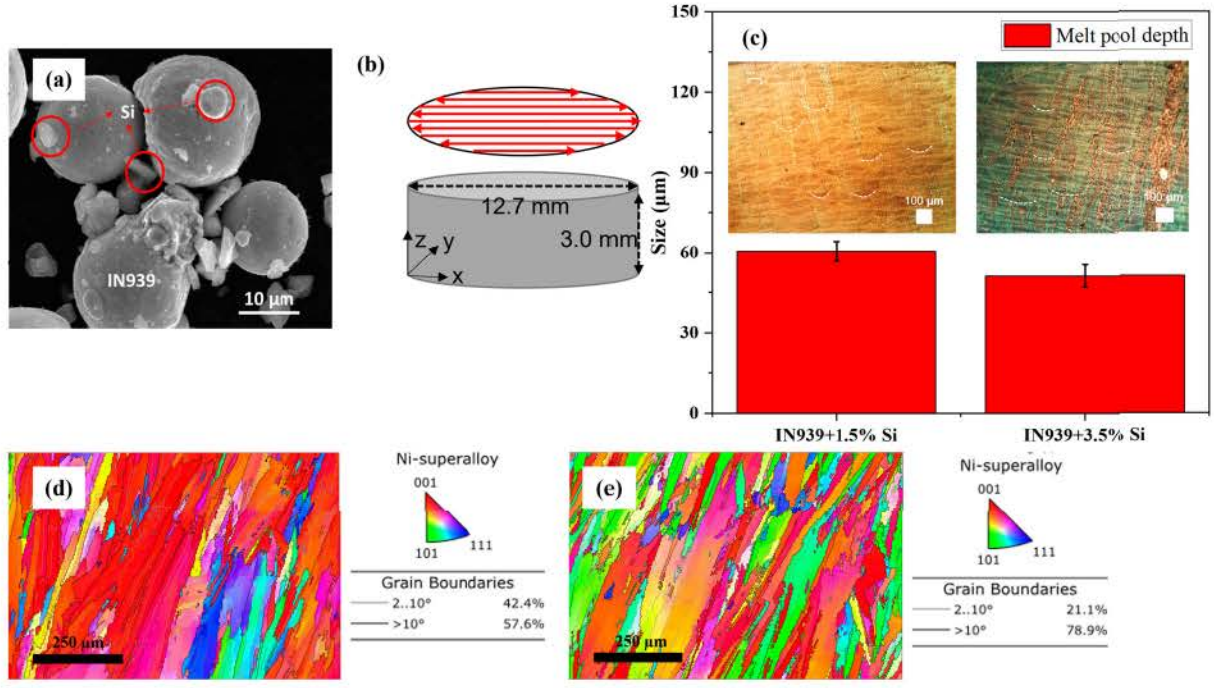

Figure 1. (a) IN939 mixed with pure Si powder (b) Scan strategy (c) Molten pool morphology and size (d) Inverse pole figure of the IN939 cross-section (parallel building direction) (e) Inverse pole figure of the IN35 cross-section.

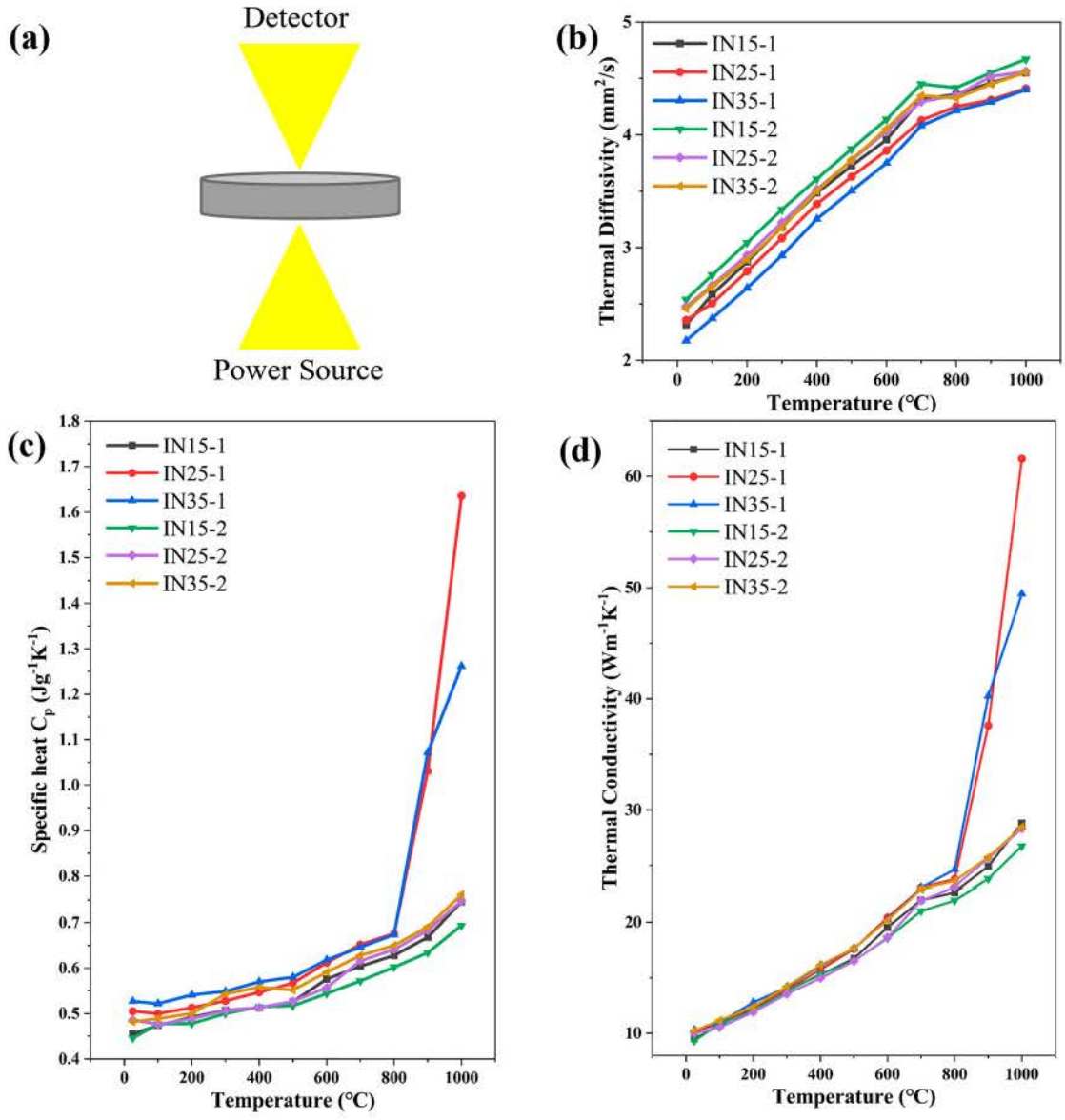

Figure 2. Thermal properties of different IN939 as-fabricated samples. (a) Schematic diagram of the thermal test. (b) Thermal Diffusivity. (c) Specific Heat. (d) Thermal Conductivity.

sample. Measured with the Archimedes' method, densities of the as-fabricated IN15, IN25, and IN35 samples are 8.25 ± 0.03, 8.23 ± 0.09, 8.22 ± 0.11 g/cm^3, respectively. As shown in Figure 2b, the thermal diffusivity values of all IN939 samples increase monotonically from 25 to 1000 °C. To detect the transient phenomena, the tests are repeated for a second cycle to 1000 °C after the samples are cooled down to room temperature. After the first thermal cycle, the heat treatment effect resulted in a more homogeneous microstructure leading to improved thermal diffusivity by about 6%. In Figure 2c, samples with different Si addition have almost identical thermal conductivity when the test temperature is below 500 °C. As the test temperature continues to increase (500-1000 °C), it can be observed that the thermal conductivity of the IN939 sample increases with the increase of the Si content. The difference in their thermal conductivity is no more than 7%.

The endothermic reaction induced phenomenon is that the thermal conductivity and specific heat of the as-fabricated IN25 and IN35 exhibit unusually high values at 900 and 1000 °C during the first testing cycle. This spike cannot be found in the second testing cycle. To exclude experiment-induced errors, new as-fabricated samples are prepared for the test, and again it shows similar results with different heating rates (10 and 25 °C/min). Based on equation 1, endothermic reactions entail the absorption of heat, leading to a reduction in the magnitude of temperature change. Therefore, the C_p will increase, given the absence of any change in the reference

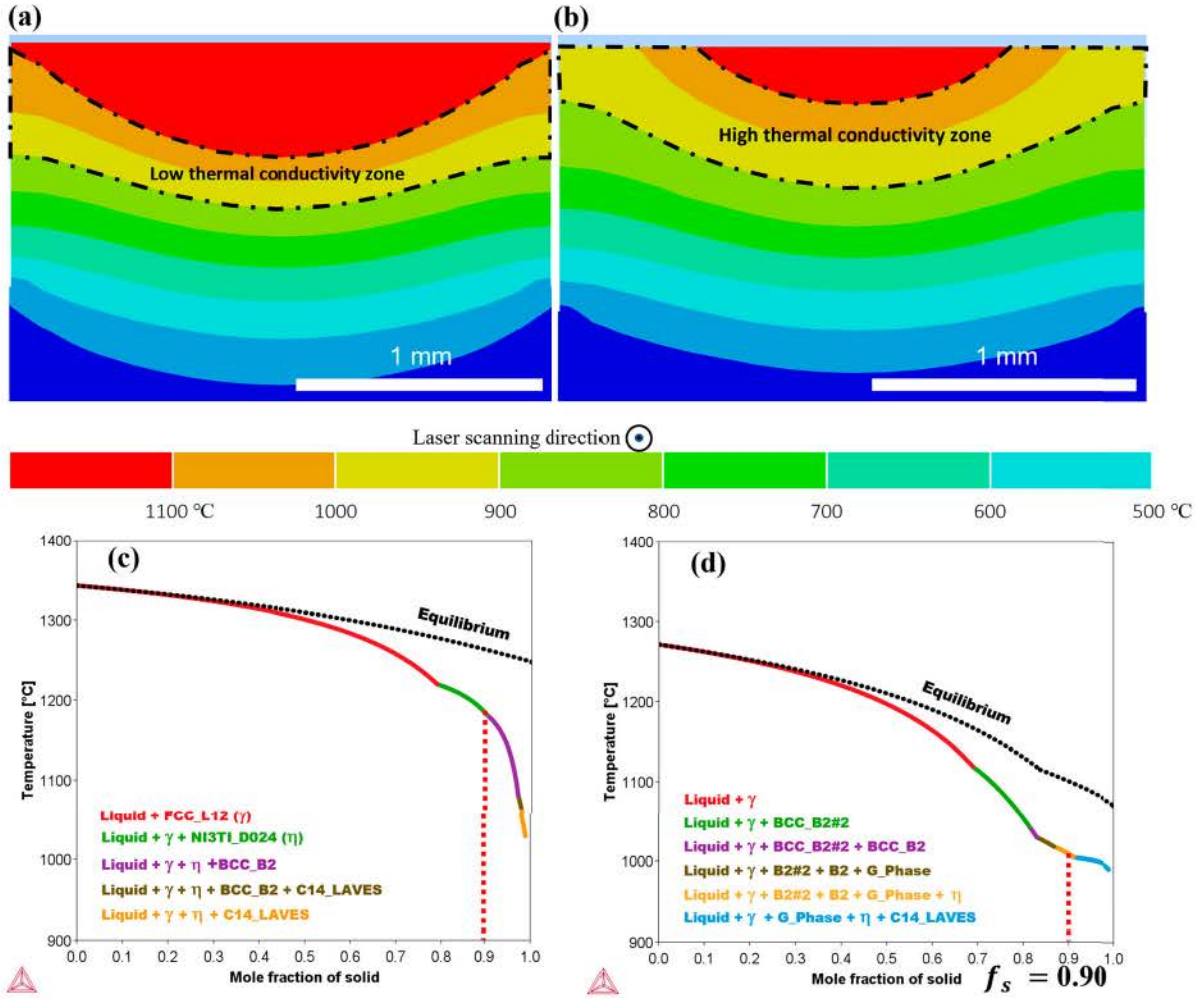

Figure 3. Schematic temperature field under L-PBF. (a) Temperature distribution of Standard thermal conductivity (IN939 without endothermic). (b) Temperature distribution of IN939 with endothermic. (c) Scheil Simulation for IN939. (d) Scheil Simulation for IN35.

sample. The residual endothermic reaction is absent during the second thermal cycle, indicating the occurrence of an even stronger endothermic reaction during the L-PBF printing process. With the super high cooling rate during the L-PBF process, the nucleation and diffusion growth of Si related phase has insufficient time to completely form. When the Si content is low (IN15), the Si-related phases almost complete the phase transformation during the L-PBF process. The temporary increase in thermal conductivity due to the endothermic reaction cannot be observed from the as-fabricated sample. As the Si content increases (IN35), the fast cooling process leads to insufficient diffusion and eventually to an incomplete endothermic reaction. In addition, after 150 min at high temperatures (based on the time of thermal property heating/testing total time), the reaction is completed. This time frame can be handled in a typical heat treatment process to give a stable L-PBF part with no more Si diffusion-related reactions. For the IN25 and IN35 samples, the complex endothermic phase transition at high temperatures drives up the C_p value, which leads to an increase in thermal conductivity. It's reasonable to believe that the same thermal behavior would also happen during the L-PBF process, and the completion of such a reaction is determined by local temperature history at high temperatures.

Figure 3a and b present the temperature distribution for samples with/without elevated thermal conductivity above 800 °C. It can be observed that the temperature gradient (over 900–1000 °C) for the high conductivity case is smaller than the standard conductivity case. The area surrounded by the black dashed line is calculated by the software ImageJ, and the area without endothermic reaction and with endothermic reaction cases was 0.578 and 1.395 mm^2, respectively. According to classic hot tearing theory [10, 15, 35], solidification cracking is a phenomenon that typically occurs in the later stages of solidification. When

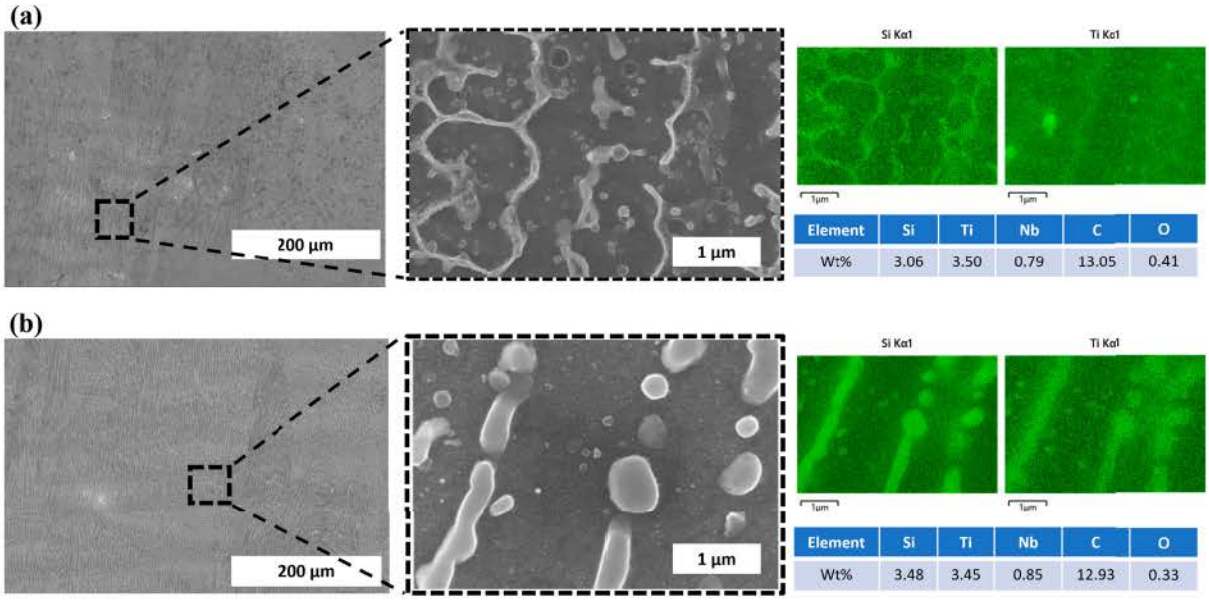

Figure 4. EDS analysis for (a) as-fabricated IN35 and (b) as-heated IN35.

the liquid phase content is between 60% and 10%, sufficient liquid feeding fills the grain gaps caused by thermal contraction, thereby reducing the material's susceptibility to cracking. This range is known as the relaxation period, denoted as t_R. When the liquid content is between 10% and 1%, the material is prone to cracking due to restricted liquid feeding. The period is referred to as the vulnerability period t_V. Figure 3c and d show the Scheil simulation of the IN939 and IN35. The temperature of the final stages of solidification ($f_s = 0.9\%-1$) of IN35 is from 900–1020 °C. The damage caused by thermal stress can be significantly reduced in this temperature range owing to the diminished thermal gradient.

The simulation and experimental results demonstrate a high consistency. The consistency mainly relates to the changes in the morphology of the melt pool, specifically the depth of the melt pool transitioning from deep to shallow. The endothermic reaction induced by Si addition could also contribute to reducing the occurrence of pore defects during the L-PBF process. The pore defects primarily originate from metal vapor generated under laser irradiation [36]. Due to the introduction of Si, an endothermic reaction occurs within the melt pool. As a result, the endothermic reaction leads to a reduction in metal vapor, thereby reducing spattering during the printing process. Simultaneously, the decrease in temperature gradient helps IN939 avoid cracking during the vulnerable period.

To further explore the endothermic phase transition, EDS was used to quantify the changes in Si content in the samples before and after thermal cycling. Figure 4a and b show the EDS mapping of the etched as-fabricated and as-heated IN35 samples. In as-fabricated IN35, incomplete diffusion of Si caused by rapid cooling resulted in insufficient phase transformation, leading to fewer overlapping regions between Si and Ti elements. Si was present in a solid-solution form within the matrix, and the overall Si content (3.05%) was lower than the initially added Si content (3.5%). After undergoing high-temperature thermal cycling, the diffusion phase transformation of Si was essentially completed, as shown in the EDS mapping in Figure 4b, demonstrating a complete overlap between Si and Ti. It is worth noting that as-heated IN35 exhibits a significant presence of nano-sized precipitates within the matrix. In the future, Transmission Electron Microscopy (TEM) may be required for further characterization of these substances.

Figure 5a and b shows the XRD pattern of the as-fabricated and as-heated (after the first thermal measurement cycle) sample with different Si content. It can be observed that the diffraction peaks in the as-heated sample shift towards larger angles as compared to the as-fabricated sample. According to Bragg's equation, that indicates the migration of solute atoms from the matrix phase to form the precipitates. Meanwhile, the intensity of the secondary phase peak (marked by the red arrow) significantly increases after the heat cycle, which also suggests the formation of the precipitates. The main component of the secondary phase is $(Ni, Co, Ti, Al)_{16}(Ti, Nb)_6Si_7$. The endothermic reactions peak in the as-fabricated IN35 sample (IN35-1) is observed at 1010 °C in the DSC test, and the starting temperature at which the

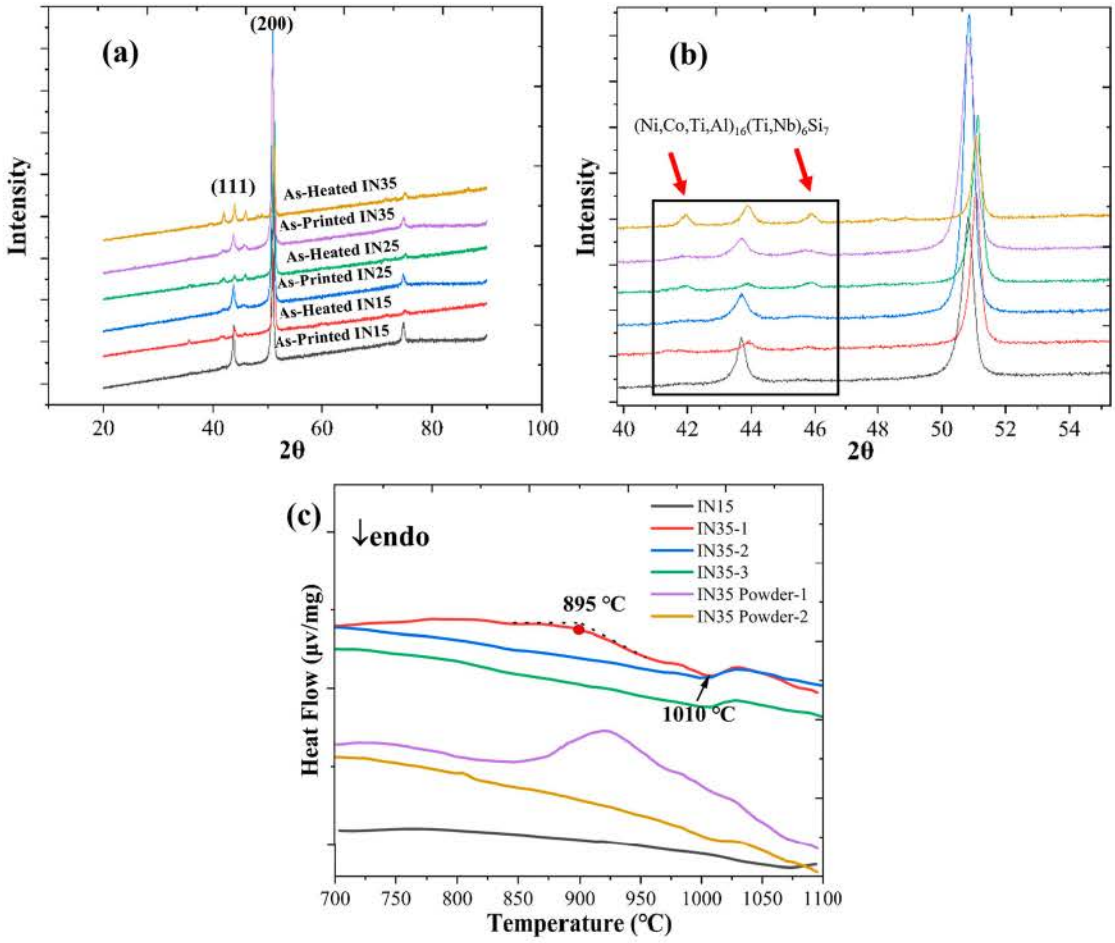

Figure 5. XRD and DSC curve of different IN939 samples before and after thermal test. (a) scans over the 2θ angle range of 20°–90°. (b) scans over a narrow 2θ angle range of 40°–50°. (c) DSC curve from 700 °C to 1100 °C.

reaction takes place is about 895 °C, as shown in Figure 4c. In the second and third thermal cycles (IN35-2 and IN35-3), the endothermic peak of the sample is significantly weakened. The DSC curve of the third cycle is almost the same as the second cycle, which indicates the homogeneity of the sample. Similar results are found with the compressed IN35 raw powder. In the first thermal cycle (IN35 powder-1), the endothermic peak is observed at about 850 °C. In the second thermal cycle, no peak can be detected between the 700–1100 °C range.

4. Conclusion

In summary, diverging from traditional researchers who utilize modified pre-alloyed powders in the gas-atomized form directly, Si was incorporated into the IN939 gas-atomized powder through mechanical mixing in our paper, resulting in an endothermic phase transition reaction during the L-PBF process. This study demonstrated that the endothermic process associated with new phase formation may be explored for reducing thermal stress in the L-PBF process, thus improving the weldability of L-PBF alloys. Although we did not observe specific instances of endothermic reactions at the experimental level, this endothermic reaction exists in the crack-free alloy of IN939 + Si, and this potential reduction in thermal gradients contributes positively to the reduction of thermal stress. Also, the trend of grain growth along the building direction is altered by the existence of an endothermic reaction. Under conditions of diminished thermal gradient, the selective orientation of columnar crystals decreases, while the number of large-angle grain boundaries increases. The endothermic reaction for the IN939 and Si powder mixture was confirmed by DSC. Further experiments are necessary to establish the dependability of new element addition. Employing this powder design strategy not only decreases the research expenses but also could play a significant part in mitigating crack formation for any other nonweldable alloy.

Disclosure statement

No potential conflict of interest was reported by the author(s).

Funding

This work is supported by the National Science Foundation (Grant Number NSF #OIA-2118756). The use of instruments housed within the LSU Shared Instrumentation Facilities (SIF), a part of LAMDA (Grant Number NSF #OIA-1946231) Core User Facilities, is acknowledged.

References

[1] Khairallah SA, Anderson AT, Rubenchik A, et al. Laser powder-bed fusion additive manufacturing: physics of complex melt flow and formation mechanisms of pores, spatter, and denudation zones. Acta Mater. 2016;108:36–45. doi:10.1016/j.actamat.2016.02.014

[2] Bi G, Gasser A. Restoration of nickel-base turbine blade knife-edges with controlled laser aided additive manufacturing. Phys Procedia. 2011;12:402–409. doi:10.1016/j.phpro.2011.03.051

[3] Zeng C, Ghadimi H, Ding H, et al. Microstructure evolution of Al6061 alloy made by additive friction stir deposition. Materials (Basel). 2022;15(10):3676. doi:10.3390/ma15103676

[4] Zeng C, Wen H, Bernard BC, et al. Tensile properties of additively manufactured C-18150 copper alloys. Met Mater Int. 2022;28(1). doi:10.1007/s12540-021-01052-0

[5] Liu S, Shin YC. Additive manufacturing of Ti6Al4V alloy: a review. Mater Des. 2019;164:107552. doi:10.1016/j.matdes.2018.107552

[6] Saboori A, Aversa A, Marchese G, et al. Microstructure and mechanical properties of AISI 316L produced by directed energy deposition-based additive manufacturing: a review. Appl Sci. 2020;10(9):3310. doi:10.3390/app10093310

[7] Ding H, Zeng C, Raush J, et al. Developing fused deposition modeling additive manufacturing processing strategies for aluminum alloy 7075: sample preparation and metallographic characterization. Materials (Basel). 2022;15(4).1340. doi:10.3390/ma15041340.

[8] Wang X, Gong X, Chou K. Review on powder-bed laser additive manufacturing of Inconel 718 parts. Proc Inst Mech Eng B J Eng Manuf. 2017;231(11):1890–1903. doi:10.1177/0954405415619883

[9] Catchpole-Smith S, Aboulkhair N, Parry L, et al. Fractal scan strategies for selective laser melting of 'unweldable'nickel superalloys. Addit Manuf. 2017;15:113–122. doi:10.1016/j.addma.2017.02.002.

[10] Zeng C, Ding H, Bhandari U, et al. Design of crack-free laser additive manufactured Inconel 939 alloy driven by computational thermodynamics method. MRS Commun. 2022;12(5):844–849. doi:10.1557/s43579-022-00253-x

[11] Li Y, Liang X, Yu Y, et al. Microstructures and mechanical properties evolution of IN939 alloy during electron beam selective melting process. J Alloys Compd. 2021;883:160934. doi:10.1016/j.jallcom.2021.160934

[12] Tang YT, Panwisawas C, Ghoussoub JN, et al. Alloys-by-design: application to new superalloys for additive manufacturing. Acta Mater. 2021;202:417–436. doi:10.1016/j.actamat.2020.09.023

[13] Chauvet E, Kontis P, Jägle EA, et al. Hot cracking mechanism affecting a non-weldable Ni-based superalloy produced by selective electron beam melting. Acta Mater. 2018;142:82–94. doi:10.1016/j.actamat.2017.09.047

[14] Rappaz M, Drezet JM, Gremaud M. A new hot-tearing criterion. Metall Mater Trans A. 1999;30:449–455. doi:10.1007/s11661-999-0334-z.

[15] Kou S. A criterion for cracking during solidification. Acta Mater. 2015;88:366–374. doi:10.1016/j.actamat.2015.01.034

[16] Yu W, Xiao Z, Zhang X, et al. Processing and characterization of crack-free 7075 aluminum alloys with elemental Zr modification by laser powder bed fusion. Mater Sci Addit Manuf. 2022;1(1):4. doi:10.18063/msam.v1i1.4

[17] Zhou W, Tian Y, Tan Q, et al. Effect of carbon content on the microstructure, tensile properties and cracking susceptibility of IN738 superalloy processed by laser powder bed fusion. Addit Manuf. 2022;58:103016. doi:10.1016/j.addma.2022.103016.

[18] Koh HK, Moo JGS, Sing SL, et al. Use of fumed silica nanostructured additives in selective laser melting and fabrication of steel matrix nanocomposites. Materials (Basel). 2022;15(5):1869. doi:10.3390/ma15051869

[19] Bertoli US, MacDonald BE, Schoenung JM. Stability of cellular microstructure in laser powder bed fusion of 316L stainless steel. Mater Sci Eng A. 2019;739:109–117. doi:10.1016/j.msea.2018.10.051

[20] Mirkoohi E, Tran H-C, Lo Y-L, et al. Mechanics modeling of residual stress considering effect of preheating in laser powder bed fusion. J Manuf Mater Process. 2021;5(2):46. doi:10.3390/jmmp5020046

[21] Mosallanejad MH, Niroumand B, Aversa A, et al. In-situ alloying in laser-based additive manufacturing processes: a critical review. J Alloys Compd. 2021;872:159567. doi:10.1016/j.jallcom.2021.159567.

[22] Zhang B, Ding H, Meng AC, et al. Crack reduction in Inconel 939 with Si addition processed by laser powder bed fusion additive manufacturing. Addit Manuf. 2023;72:103623. doi:10.1016/j.addma.2023.103623.

[23] Sing SL, Huang S, Goh GD, et al. Emerging metallic systems for additive manufacturing: in-situ alloying and multi-metal processing in laser powder bed fusion. Prog Mater Sci. 2021;119:100795. doi:10.1016/j.pmatsci.2021.100795.

[24] Takata N, Liu M, Kodaira H, et al. Anomalous strengthening by supersaturated solid solutions of selectively laser melted Al–Si-based alloys. Addit Manuf. 2020;33:101152–101152. doi:10.1016/j.addma.2020.101152.

[25] Montero Sistiaga ML, Mertens R, Vrancken B, et al. Changing the alloy composition of Al7075 for better processability by selective laser melting. J Mater Process Technol. 2016;238:437–445. doi:10.1016/j.jmatprotec.2016.08.003

[26] Li G, Jadhav SD, Martín A, et al. Investigation of solidification and precipitation behavior of Si-modified 7075 aluminum alloy fabricated by laser-based powder Bed fusion. Metall Mater Trans A. 2021;52(1):194–210. doi:10.1007/s11661-020-06073-9

[27] Vilanova M, Taboada MC, Martinez-Amesti A, et al. Influence of minor alloying element additions on the crack susceptibility of a nickel based superalloy manufactured by lpbf. Materials (Basel). 2021;14(19). doi:10.3390/ma14195702

[28] Tomus D, Jarvis T, Wu X, et al. Controlling the microstructure of Hastelloy-X components manufactured by selective laser melting. Phys Procedia. 2013;41:823–827. doi:10.1016/j.phpro.2013.03.154
[29] Engeli R, Etter T, Hövel S, et al. Processability of different IN738LC powder batches by selective laser melting. J Mater Process Technol. 2016;229:484–491. doi:10.1016/j.jmatprotec.2015.09.046
[30] Cloots M, Uggowitzer PJ, Wegener K. Investigations on the microstructure and crack formation of IN738LC samples processed by selective laser melting using Gaussian and doughnut profiles. Mater Des. 2016;89:770–784. doi:10.1016/j.matdes.2015.10.027
[31] Hariharan A, Lu L, Risse J, et al. Misorientation-dependent solute enrichment at interfaces and its contribution to defect formation mechanisms during laser additive manufacturing of superalloys. Phys Rev Mater. 2019;3(12):123602. doi:10.1103/PhysRevMaterials.3.123602
[32] Zhang C, Bhandari U, Zeng C, et al. Carbide formation in refractory Mo15 Nb20 Re15 Ta30 W20 alloy under a combined high-pressure and high-temperature condition. Entropy. 2020;22(7):718. doi:10.3390/e22070718.
[33] Wen H. 2021. Laser surface treatment and laser powder bed fusion additive manufacturing study using custom designed 3D printer and the application of machine learning in materials science. Louisiana State University and Agricultural & Mechanical College.
[34] Chen Y, Zeng C, Ding H, et al. Thermophysical properties of additively manufactured (AM) GRCop-42 and GRCop-84. Materials Today Communications. 2023;36:106665. doi:10.1016/j.mtcomm.2023.106665.
[35] Clyne TW, Wolf M, Kurz W. The effect of melt composition on solidification cracking of steel, with particular reference to continuous casting. Metall Trans B. 1982;13(2):259–266. doi:10.1007/BF02664583
[36] Li Z, Li H, Yin J, et al. A review of spatter in laser powder bed fusion additive manufacturing: in situ detection, generation, effects, and countermeasures. Micromachines (Basel). 2022 Aug 22;13(8):1366. doi:10.3390/mi13081366.